5-6-2021

Rocket Flight Simulation with Monte Carlo Uncertainty Analysis

Jonathan Wallace Drake

Rocket Flight Simulation with Monte Carlo Uncertainty Analysis

by

Jonathan Wallace Drake

An Honors Capstone

submitted in partial fulfillment of the requirements

for the Honors Diploma

to

The Honors College

Of

The University of Alabama in Huntsville

6 May 2021

Honors Capstone Director: Dr. David Lineberry

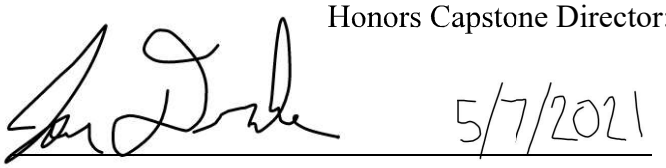

Student Date

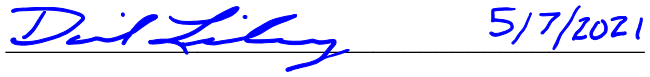

Director Date

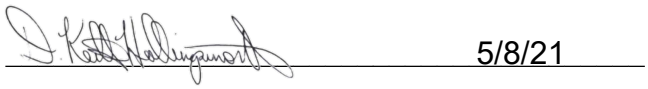

Department Chair Date

William Wilkerson

Digitally signed by William Wilkerson
Date: 2021.05.10 09:01:03 -05'00'

Honors College Dean Date

HONORS COLLEGE
THE UNIVERSITY OF ALABAMA IN HUNTSVILLE

Honors College
Frank Franz Hall
+1 (256) 824-6450 (voice)
+1 (256) 824-7339 (fax)
honors@uah.edu

Honors Thesis Copyright Permission

This form must be signed by the student and submitted with the final manuscript.
In presenting this thesis in partial fulfillment of the requirements for Honors Diploma or Certificate from The University of Alabama in Huntsville, I agree that the Library of this University shall make it freely available for inspection. I further agree that permission for extensive copying for scholarly purposes may be granted by my advisor or, in his/her absence, by the Chair of the Department, Director of the Program, or the Dean of the Honors College. It is also understood that due recognition shall be given to me and to The University of Alabama in Huntsville in any scholarly use which may be made of any material in this thesis.

Jon Drake
Student Name (printed)

Student Signature

05/7/2021
Date

Table of Contents

Dedication

This project is dedicated to the 2020-2021 Charger Rocket Works USLI Senior Design team and our rocket, the aptly named El Gigante without whom there would be no flight data for comparison.

Abstract

Like all dynamic systems, a rocket's performance is characterized by too many variables to be accurately and with a sufficient degree of confidence approximated analytically. This project outlines a numerical approach to provide a more accurate and trustworthy analysis of a rocket's flight profile. This approach uses Newtonian physics iteratively to reduce uncertainty regarding critical flight parameters necessary for design implementation. This project has embedded a Monte Carlo uncertainty analysis to capture the effects of real-world variables on the numerical outcome. The simulation produces, primarily, a characterization of the rocket's altitude, velocity, and acceleration with respect to the time of flight. It also provides insight into the stability and load expectation of the rocket. The simulation results compared to actual flight data show an accurate prediction of critical flight parameters and total Monte Carlo inclusion of each flight's outcome. Using this approximation, a rocket can be better designed to meet mission requirements or slated performance criteria.

1. Introduction

When designing a rocket, there is generally some mission profile or performance guidelines for which the rocket is responsible for meeting. Unfortunately, the complex physics governing dynamic rocket flight are difficult to predict with basic analytical methods accurately. This project provides a process for interpreting a rocket's flight profile numerically by first describing the general physics as a foundation upon which to build. The analytical approach will also be outlined to validate the performance of the simulation. However, because the simulation is intended to be more accurate than the analytics, it will also be compared to actual flight data. While the simulation more accurately predicts the rocket's performance, it does not capture some of the unpredictable aspects of a flight perfectly. A Monte Carlo uncertainty analysis is embedded into the simulation to provide a confidence interval for the expected performance.

The Monte Carlo Analysis provides a general understanding of how well a rocket can fit the performance guidelines when the exact parameters are unknown. This general understanding allows the design process to be somewhat streamlined. A range of possibilities can be simulated in the earlier stages allowing for more variations down the line. A greater understanding of the rocket's performance allows for more significant variability in design as changes in parameters like weight, and cross-sectional area can already be accounted for in the uncertainty intervals. A Monte Carlo analysis on one example of rocket flights will be shown with detailed uncertainty parameters with respective intervals.

2. Rocket Flight Basics

Within this document's confines, a rocket is a long cylindrical body with a tapered nose cone and fins at the body's base; i.e., other protruding bodies such as wings and canards are not considered. This document also deals exclusively with single-stage solid propellant rocket motors as the source of thrust. A rocket's flight can be characterized by three main phases separated by five critical points shown in**Error! Reference source not found.** Specifically, a rocket starts vertically on some launchpad until the first critical point, the launch. The launch is when the motor propellant is ignited, beginning the first phase, the powered ascent. As the solid propellant burns, the heat and pressure increase inside the motor casing forcing the resulting gases to accelerate through a nozzle at the motor's base. The gases' speed and mass as they exit the nozzle provide the necessary thrust to propel the rocket. After all the solid propellant has burned, the second critical point, motor burnout, has been reached, beginning the second phase of the flight, coasting ascent. At motor burnout, the vehicle should be at its maximum velocity, which provides the energy to continue increasing altitude. Neglecting lift, the only remaining forces during the coasting phase are drag and gravity, both of which oppose the rocket's motion. As a result, the rocket begins decelerating until it reaches zero vertical velocity. Apogee is the third critical point which is the highest altitude the rocket achieves during flight. As the rocket then begins to descend back towards Earth, it enters the third and final phase, recovery. Typically, a parachute or streamer is used to increase the rocket's drag coefficient as it descends, thereby reducing the descent velocity.

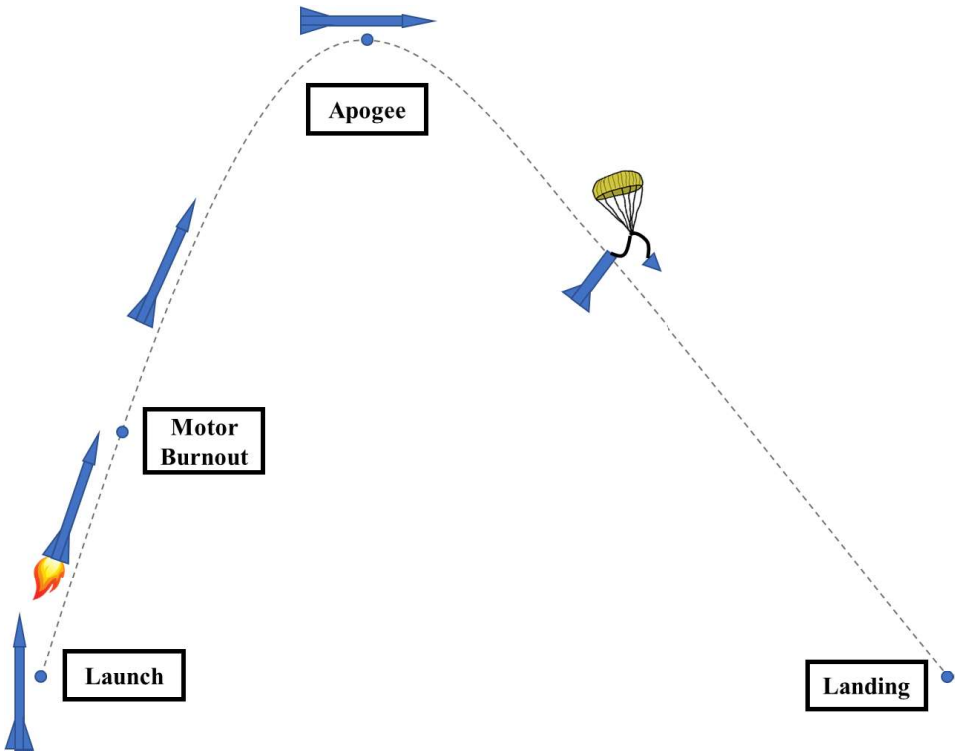

Figure 1: Basic Flight Phases

The parachute or streamer is stored inside the rocket's body until some criteria are met. Potential criteria could be apogee or a predetermined altitude. To deploy the parachutes, small pyrotechnic charges or pressurized gas canisters are used to separate the rocket body at designed split points. Recovery can also be split into different phases; for instance, this document deals with a dual recovery system where a small parachute is deployed at apogee and a larger parachute deployed at a lower altitude. A larger parachute reduces the impact energy of the rocket at the fifth critical point, landing. Unfortunately, a larger parachute deployed at apogee can result in more significant wind drift. However, too small of a parachute at apogee can result in either too great an impulse when a larger parachute is deployed later or too high impact energies on landing. Optimizing these concerns will also be discussed.

2.1. Flight Forces

The primary forces acting on the rocket during a flight are thrust, drag, and gravity, shown in Figure 2. Lift is also a contributing force but will be explained in Section 2.3. For thrust, this document deals with solid propellant rocket motors. Commercial hobby class solid rocket motors are characterized by classes based on total impulse ranges, average thrust value, type of propellant, and delay charges. For instance, the L1390G Aerotech rocket motor used with all example rockets for this project is an L class total impulse range with an average thrust of 1390 Newtons. The propellant used is Mojave Green with no delay charge.

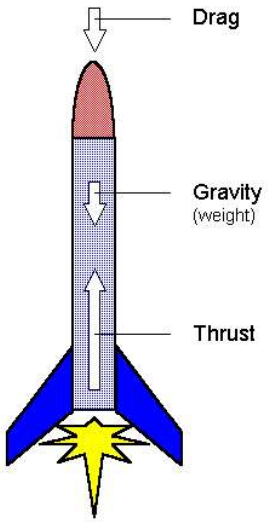

Figure 2: Powered Ascent Phase Force Diagram

The total impulse classes are broken up by letter starting with a class 'A' motor having a total impulse range from 1.26-2.5 Ns. Subsequent letters double the allowable range of total impulse. Table 1 shows some of the classifications with respective total impulse ranges.

Table 1: Total Impulse Classification

Class	Total Impulse (Ns)	Class	Total Impulse (Ns)	Class	Total Impulse (Ns)
A	1.26-2.50	E	20.01-40.0	I	320.01-640
B	2.51-5.00	F	40.01-80.0	J	640.01-1280
C	5.01-10.0	G	80.01-160	K	1280.01-2560
D	10.01-20.0	H	160.01-320	L	2560.01-5120

Total impulse by itself does not reveal how well a motor performs. Total impulse is the integral of total thrust with respect to time, as shown in Eq. 1, where F is the thrust as a function of time, t_b, is the burn time of the motor, and I is the total impulse.

$$I = \int_0^{t_b} F\,dt \qquad \text{Eq. 1}$$

A higher value typically means higher thrust, but more propellant is often added to achieve a greater thrust in some motors. Increasing the propellant increases the motor's overall mass, which negates some of the higher thrust benefits. To better represent the rocket motor's efficiency, the total impulse is divided by the propellant's weight to get the specific impulse. Eq. 2 shows the specific impulse calculation where $m_p(t)$ is the propellant mass at some time t, and g is the gravitational constant.

$$I_{sp} = \frac{I}{m_p(t)g} \qquad \text{Eq. 2}$$

The specific impulse is a measure of how efficiently a motor can generate thrust from a certain mass of propellant. The specific impulse is used to represent the thrust in Newton's simple force balance. Eq. 3 depicts the force balance using the free body diagram in Figure 2.

$$m\frac{dv}{dt} = -mg - D + \dot{m}_p g I_{sp} \qquad \text{Eq. 3}$$

$\dot{m}_p$ is the propellant mass flow rate (dm_p/dt) or the rate of propellant mass change with respect to time, m is the current mass of the system at any given time, and D is the drag force. As will be explained in section 3, Eq. 3 can be iterated numerically to deal with the time-dependent parameters. However, to solve analytically as a method for validating the simulation, the drag force is neglected (for now), divide both sides by mass, and multiplied by dt resulting in Eq. 4.

$$dv = -gdt + \frac{dm}{m} gI_{sp} \quad \text{Eq. 4}$$

Both sides of Eq. 4 can be integrated, assuming gravity, specific impulse, and $\dot{m}_p$ are constant, resulting in Eq. 5.

$$\Delta v = -gt_b + \ln\left(\frac{m_o}{m_f}\right) gI_{sp} \quad \text{Eq. 5}$$

$\frac{m_o}{m_f}$ is the initial, total mass of the rocket divided by the burnout mass or the initial mass minus the propellant mass. The time of burnout or the duration of the motor burn is t_b. Eq. 5 produces a resulting change in velocity after an engine burn. Because this document considers a single-stage solid-propellant motor, the powered ascent phase is the only phase characterized by this equation, and the initial velocity at launch is zero. Therefore, the Δv from the initial burn is the maximum velocity, or burnout velocity. Realistically, using Eq. 5 to predict the burnout velocity is inaccurate when assuming negligible drag.

Drag is challenging to simplify as it is dependent on the vehicle's velocity squared, which is not constant during the powered ascent phase. Therefore, to truly validate the simulation, an estimated percent reduction in apogee will be applied to the final calculations to represent the effects of drag on the overall flight profile. In that regard, to now determine the height of the rocket at motor burnout, Eq. 5 can be adjusted to determine the velocity at any time between launch when velocity is zero and t_b.

$$v(t) = -gt + \ln\left(\frac{m_o}{m_o - \dot{m}_p t}\right) gI_{sp} \quad \text{Eq. 6}$$

Assuming the mass flow rate is constant, the mass at time t is the initial mass minus the mass flow rate times t. This value gives the mass at time t, and in Eq. 6 can be seen to equal m_f when t is t_b. With everything now defined as a function of time, Eq. 6 can now be integrated on the interval $0 < t < t_b$ to get Eq. 7

$$h_b = -\frac{1}{2} g t_b^2 - g t_b Isp \frac{\ln\left(\frac{m_o}{m_f}\right)}{\frac{m_o}{m_f} - 1} + g t_b Isp \quad \text{Eq. 7}$$

h_b represents the height of the rocket at burnout, assuming vertical flight and negligible drag again. Using the equation for energy conservation and recognizing that drag is not

performing work on the rocket, the rocket's potential and kinetic energies can reveal the height at apogee.

$$h_a = h_b + \frac{v_b^2}{2g} \quad \text{Eq. 8}$$

Eq. 8 shows this application. h_a is the rocket's height at apogee and v_b is the burnout velocity, which is Δv is the launch velocity is zero. As mentioned, Eq. 4-8 are simplifications of the actual physics governing a flight. Specifically, ignoring drag provides a severe misconception of a realistic expectation for an apogee. Considering that the analytical solution is meant to validate the simulation results, the drag must be factored into the final result. Eq. 9 derives a drag influence number, N using previously stated parameters, D, the diameter of the rocket in inches, and C_d, the estimated drag coefficient.

$$N = \frac{23 C_d D^2 v_b^2}{17395 m_f} \quad \text{Eq. 9}$$

The value $\frac{23}{17395}$ is the unit conversion value for a rocket diameter in inches, a velocity in ft/s, and a final mass in lbf. The drag influence number can then be found on the x-axis of the graph in Figure 3 to find the drag reduction factors for critical parameters. Drag reduction factors represent the percentage of the analytical value that can be reasonably expected if drag is not negligible

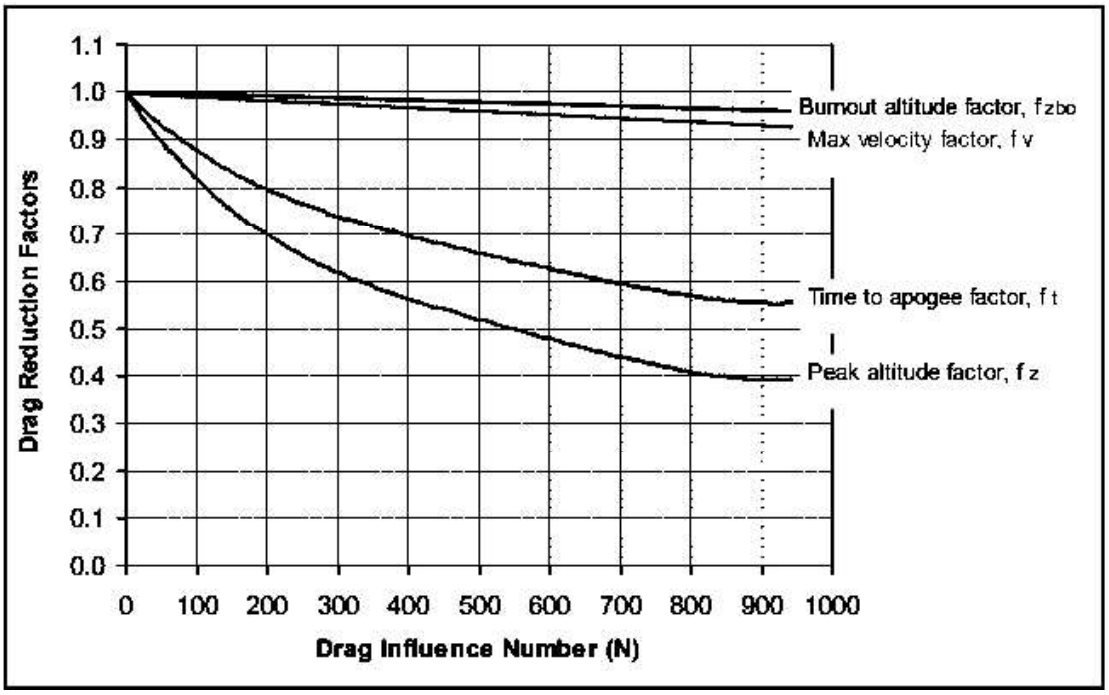

Figure 3: Drag Reduction Factor Chart [8]

2.2. Analytical Verification

With the analytical verification model setup, an actual rocket can be applied to calculate an expected flight profile up to apogee. The numerical simulation will show flights from multiple rocket designs created and flown by the 2020-2021 Charger Rocket Works USLI Competition team, the first of which is the validating model. Table 2 shows the parameters for the analytical validation rocket.

Table 2: Validation Flight Parameters

Parameter	Variable	Value
Weight	W	49 lbs
Diameter	d	6.17 in
Total Impulse	I	887.8 $lb \cdot s$
Specific Impulse	I_{sp}	204.1 s
Burn Time	t_b	2.91 s
Thrust	T	312.5 lbs
Propellant Weight	m_p	4.35 lbs
Drag Coefficient	C_d	0.42
Length	L	102 in

The critical flight parameters can be calculated assuming negligible drag, shown in Table 3 using Table 2 and the equations in section 2.1.

Table 3: Theoretical flight parameters assuming negligible drag

Parameter	Variable	Value
Burnout Height	h_b	$739\ ft$
Burnout Velocity	v_b	$517.3\ ft/s$
Apogee	h_a	$4894\ ft$

Using the burnout velocity in Table 3 and Eq. 9, the drag influence number is calculated to be 127. The drag reduction factor for each parameter in Table 3 is found using Figure 3 with the drag influence number.

Table 4: Theoretical flight parameters with drag reduction

Parameter	Drag Factor	Value
Burnout Height	0.999	$738\ ft$
Burnout Velocity	0.99	$512.1\ ft/s$
Apogee	0.8	$3915\ ft$

The values in Table 4 are the analytical predictions for the rocket whose parameters are listed in Table 2. Note that the drag reduction factors for burnout height and burnout velocity are negligible at this drag influence number, but values have been chosen that reflect slight changes. The numerical simulation of the rocket's flight is intended to be more accurate than the analytical solutions; thus, when comparing the outcome of the simulation to the values in Table 2, some discrepancy is expected. Nevertheless, the analytical solution provides a relative accuracy to target.

2.3. Rocket Stability

Another inaccurate assumption of the analytical solution is that the rocket remains vertical during its entire flight, meaning it is strictly one-dimensional motion. However, like all dynamic, ballistic projectiles, a rocket operates with 6 degrees of freedom in 3-dimensional space. Ideally, all 6 DOF would be incorporated into the simulation to provide maximum accuracy. However, this document only details 3 DOF for simplification purposes, specifically the vertical direction, the horizontal direction (without distinction), and pitch within the plane created by these two directions.

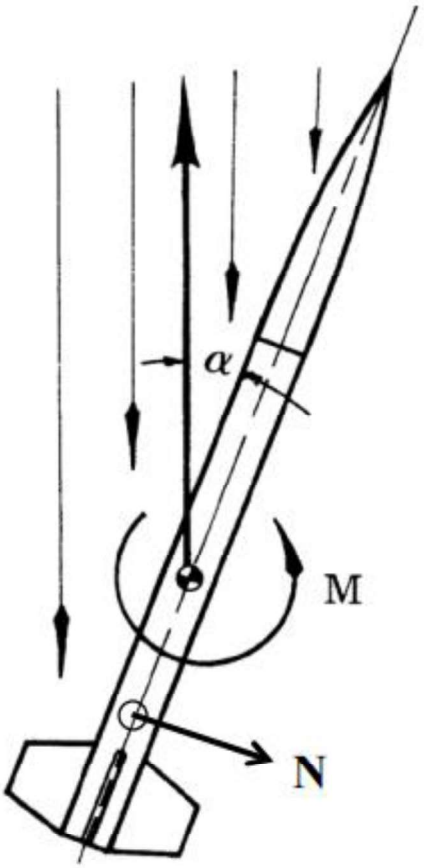

Figure 4: 3 DOF free body diagram [7]

Figure 4 is the representation of the 3 DOF represented by the simulation. The addition of the horizontal direction and pitch introduces the lift force into the characterization of the rocket's flight. Lift, or $Ncos(\alpha)$ in Figure 4, is caused by a relative velocity vector not parallel to the longitudinal axis of the rocket. Initially, the increase in the angle of attack, or the angle between the relative velocity and the longitudinal axis, is due to crosswinds.

Nevertheless, the rocket begins rotating about the center of gravity due to a moment created by the lift force acting through the center of pressure. As shown in Figure 4, the moment is acting opposite to the rotation of the rocket meaning the change in α, or angle of attack, is negative. Therefore, the rocket is stable and will tend towards $\alpha = 0$. Adversely, if the center of pressure were in front of the center of gravity, the rocket would be unstable. Because the rocket's stability is crucial for a steady flight, this simulation also has an embedded stability estimate. Specifically, the distance between the center of gravity, CG, and the center of pressure, CP, will be estimated and normalized by the rocket's diameter to get a value in calibers. CG is relatively easy to calculate; it is the point about which the body rotates, which can be found by assembling the rocket and finding the point along the longitudinal axis where the entire rocket can be supported without rotating. The CP, however, is more difficult to predict.

James and Judith Barrowman presented a paper at NARAM-8 detailing a method for predicting the location of the center of pressure with some uncertainty for incompressible flight. They effectively stripped the rocket down and detailed the effects of each part before recombining everything. The parts outlined were the nose, the cylindrical body, body transitions (where the body changes diameter over some distance), and the fins. Because the rockets detailed in this document have no body transitions, their contribution to stability is neglected. The Barrowman's also assumed small angles of attack, which reduces the contribution of the cylindrical body to 0. Therefore, the only meaningful contributions to the rocket's stability are the nose cone and the fins.

When initially presented, the Barrowman paper dealt mainly with traditional ogive and conical nose cones and trapezoidal fins. This document deals with rockets having an elliptical nose cone and elliptical fins. Fortunately, the Barrowmans' issued an addendum including a coarse method for determining the effects of elliptical fins, but not an elliptical nose cone. To that effect, greater uncertainty is placed on the nose cone contribution.

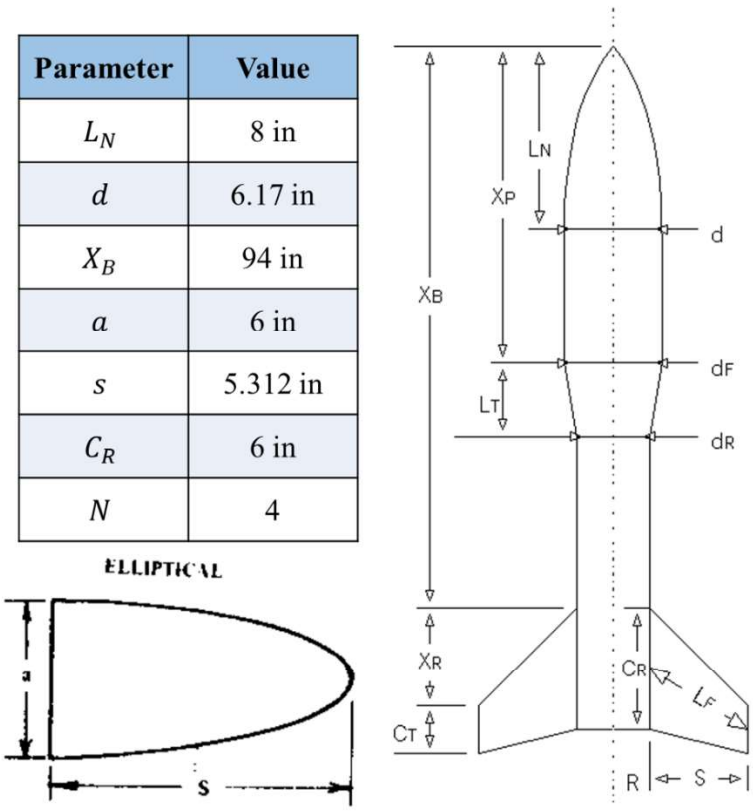

Parameter	Value
L_N	8 in
d	6.17 in
X_B	94 in
a	6 in
s	5.312 in
C_R	6 in
N	4

Figure 5: Barrowman equation parameters [1]

Figure 5 shows the parameters associated with the Barrowman equations. The lower left diagram is an elliptical fin layout. The values are congruent with the validation rocket from section 2.2. All parameters are labeled in Figure 5 except for N, which represents the number of fins. Beginning with the nose cone, Eq. 10 and Eq. 11 are used to calculate the coefficient of normal force and the location of the nose cone's center of pressure, respectively.

$$(C_N)_N = 2 \quad \text{Eq. 10}$$

$$X_N = 0.5(L_N) \quad \text{Eq. 11}$$

Barrowman assumed small angles of attack and nose cones with zero cross-sectional area at the tip that the normal force coefficient was 2. The location of the center of pressure for the elliptical nose cone is based on its geometry.

Eq. 12 and Eq. 13 do the same thing for the fins where N is the number of fins, calculating the normal force coefficient and the location of the fins center of pressure. Note that the location of both the nose cone and fin center of pressures is relative to the tip of the nose cone.

$$(C_N)_F = \frac{4N\left(\frac{s}{d}\right)^2}{1 + \sqrt{1 + 1.623\left(\frac{s}{a}\right)^2}} \quad \text{Eq. 12}$$

$$X_f = X_B + 0.288a \quad \text{Eq. 13}$$

Eq. 13 assumes the quarter chord on the mean aerodynamic chord is the center of pressure for the fins and that it is located at 28.8% the distance from the top of the root chord. A more accurate method was tested to find the exact location of the quarter chord on the mean aerodynamic chord, but the differences were negligible; thus, Eq. 13 suffices.

Now, the rocket parts can be reassembled, and the final CP location can be calculated using the contributions of each part. Eq. 14 is the equivalent normal force coefficient which is just a summation of each contributing piece. Note that if a rocket had a body transition, its contribution would also be added.

$$(C_N)_R = (C_N)_N + (C_N)_F \quad \text{Eq. 14}$$

$$\overline{X} = \frac{(C_N)_N X_N + (C_N)_F X_F}{(C_N)_R} \qquad \text{Eq. 15}$$

Eq. 15 results in the final location of the rocket's CP, $\overline{X}$. The value using the validation rocket is 68.7 inches from the tip of the nose cone. The measured center of gravity for the same rocket was 57.3 inches resulting in a normalized stability margin of 1.85 calibers. The positive number signifies that the CP is aft of the CG, meaning this rocket is stable.

3. Rocket Flight Simulation

The rocket flight simulation intends to provide a more accurate expectation of a rocket's performance than the analytical method. To that extent, the simulation is broken down into each stage of the flight, as described in section 0. Each stage employs various numerical methods to maximize the accuracy of the simulation.

3.1. Powered Ascent

The powered ascent phase, detailed in section 2, is characterized primarily by the thrust provided by the motor to the rocket, allowing the rocket to accelerate upward. A solid-propellant motor typically contains multiple propellant grains with a circular outer profile and a hollowed center with some cross-sectional area. The motor's thrust profile depends on the propellant formulation, the chamber pressure, and the burning surface area.

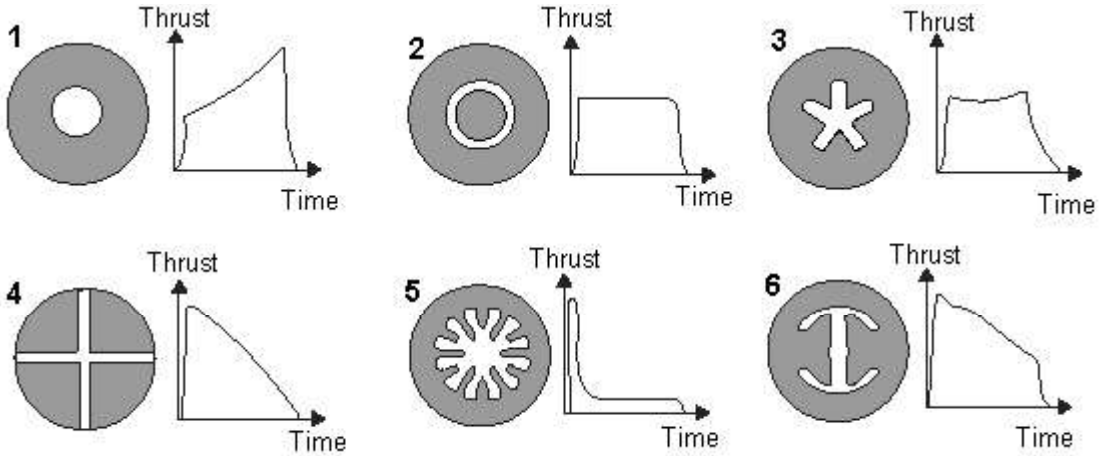

Figure 6: Solid Propellant Grain Cross-Sections

Figure 6 shows six examples of what a propellant grain cross-section may look like and the thrust profile associated with these grain geometries. The igniter is used to light the inside of the grain, the hollowed-out portion. The grain burns inside out until the outer diameter is reached. As a result, the propellant mass decreases as the motor burns until motor burnout, when there is no propellant left. The analytical method simplifies this process by assuming the mass flow rate of the motor is a constant derived from the average thrust of the motor. The thrust curves in Figure

6 show how that can be an oversimplified assumption as the thrust profile may not be characterized well by a constant.

At each time step, the simulation uses the specific impulse and thrust to determine the mass flow rate to capture the complexity of the mass of propellant reducing with time. Eq. 16 shows this seemingly simple concept.

$$\dot{m}(t) = \frac{T(t)}{I_{sp}} \qquad \text{Eq. 16}$$

The motor's specific impulse is assumed to be constant; thus, the only variable is the thrust at each time step. The thrust curve data for most commercial solid propellant motors is readily available online. Unfortunately, the data is relatively coarse for the accuracy desired by this simulation and often with unequal time steps between data points. The provided data must be interpolated with equidistant time steps equal to that of the simulation to achieve this. A third-order Lagrangian interpolation was used, which means a 3rd order polynomial is used to fit 4 data points. Figure 7 shows the visual representation of this concept.

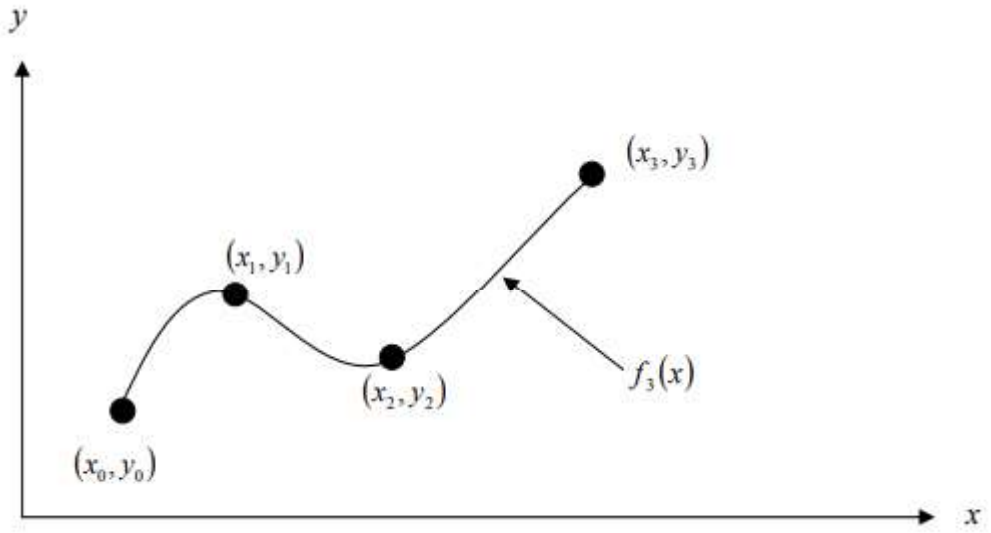

Figure 7: 3rd Order Lagrangian Interpolation [4]

The Lagrangian method uses weights of the 4 points selected, which are best applied if the selected data bracket the desired point. For instance, Figure 7 shows a third-order polynomial ($f_3(x)$) that would be used to determine any value between states 1 and 2. That is because states 0 and 1 fall strictly to the left of these values and states 2 and 3 to the right.

$$T(t) = \left(\frac{t-t_1}{t_0-t_1}\right)\left(\frac{t-t_2}{t_0-t_2}\right)\left(\frac{t-t_3}{t_0-t_3}\right)T(t_0) + \left(\frac{t-t_0}{t_1-t_0}\right)\left(\frac{t-t_2}{t_1-t_2}\right)\left(\frac{t-t_3}{t_1-t_3}\right)T(t_1) + \left(\frac{t-t_0}{t_2-t_0}\right)\left(\frac{t-t_1}{t_2-t_1}\right)\left(\frac{t-t_3}{t_0-t_3}\right)T(t_2) + \left(\frac{t-t_0}{t_3-t_0}\right)\left(\frac{t-t_1}{t_3-t_1}\right)\left(\frac{t-t_2}{t_3-t_2}\right)T(t_3) \quad \text{Eq. 17}$$

Figure 8 shows the result when the Lagrangian interpolation is applied to actual thrust data. The motor represented is the L1390G Aerotech motor used in all rockets being analyzed in this document.

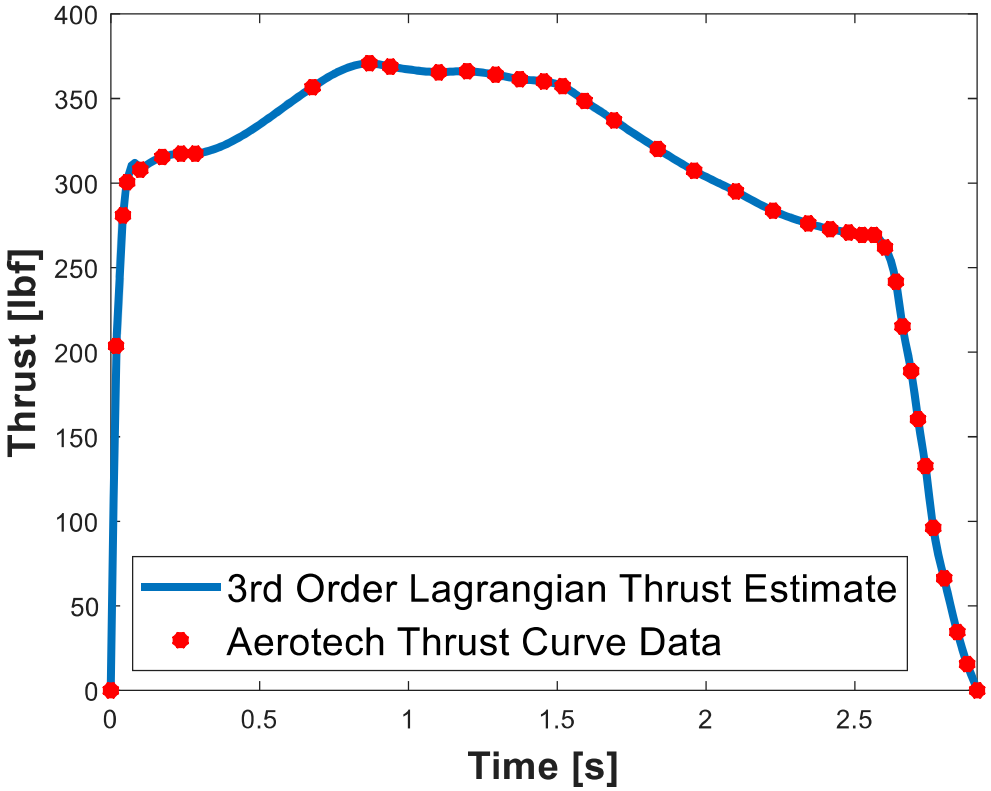

Figure 8: L1390G Aerotech Solid Rocket Motor Thrust Data

Now that the thrust data has been interpolated to the desired time step. The iteration over the powered ascent phase can begin. The process begins by taking the thrust at the given instant in time, then finding the instantaneous mass flow rate using Eq. 16. The mass flow rate can be multiplied by the time step to find the loss in mass. The current mass of the rocket is the mass from the previous time step minus the loss in mass. The next step is to use Eq. 3 to determine the acceleration. However, unlike the analytical method, the simulation actively determines the drag contribution to the net force on the rocket and, subsequently, the acceleration. It is also important to note that this simulation is implementing the 2-D motion, which means the angle of attack α, sideslip angle ψ, and relative angle from horizontal θ is used in the directionality of forces.

Figure 9 shows the directionality of these forces. Note that for this simulation, the rocket fins are symmetric with no fixed angle of attack, so the plane of the wing is coplanar with the thrust direction when ψ is zero degrees.

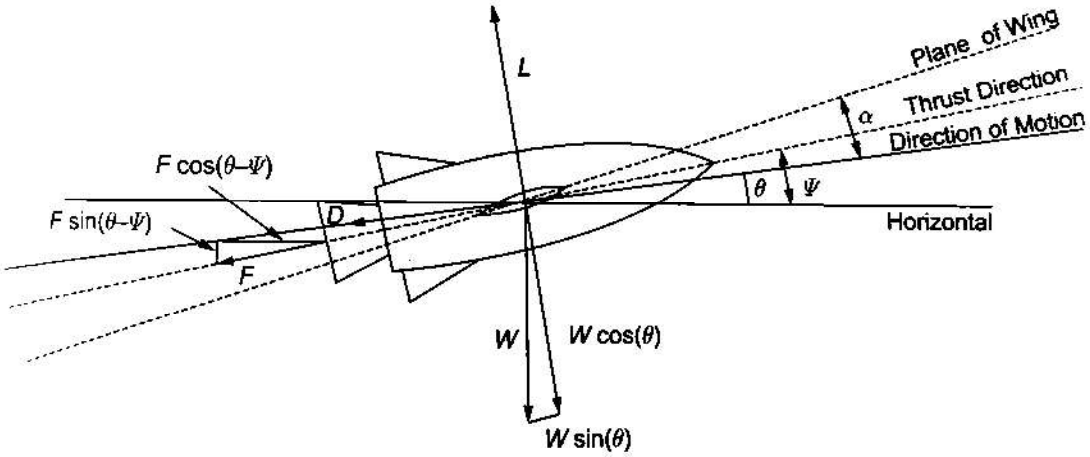

Figure 9: Forces on a rocket in generalized 2-D flight [2]

Using Eq. 18, the instantaneous drag can be calculated; where ρ is the ambient air density, A is the cross-sectional area of the rocket, V is the previous velocity of the rocket, and C_d is the drag coefficient.

$$D = \frac{1}{2}\rho V^2 A C_d \qquad \text{Eq. 18}$$

The acceleration is then the summation of the drag, weight, and thrust (with respective directions), divided by the mass. Acceleration is, by definition, the rate of change of velocity with respect to time. Thus, a numerical integration method must be used to determine the velocity. As this simulation is intended to maximize accuracy, a 4th order Runge-Kutta method was chosen. The Runge-Kutta method calculates acceleration 4 times and uses a weight method with all 4 to determine a more accurate approximation of acceleration.

$$k_1 = f(t_n, y_n) \qquad \text{Eq. 19}$$

$$k_2 = f\left(t_n + \frac{dt}{2}, y_n + \frac{dt(k_1)}{2}\right) \qquad \text{Eq. 20}$$

$$k_3 = f\left(t_n + \frac{dt}{2}, y_n + \frac{dt(k_2)}{2}\right) \quad \text{Eq. 21}$$

$$k_4 = f(t_n + dt, y_n + dt(k_3)) \quad \text{Eq. 22}$$

$$k_n = \frac{dt}{6}(k_1 + k_2 + k_3 + k_4) \quad \text{Eq. 23}$$

Eq. 19-23 show the Runge-Kutta process using the current time t_n, and adding steps, dt, to it to calculate the derivative, k, at those steps and ultimately use Eq. 23 with all the approximated derivatives to find the most accurate approximation.

Using the initial calculation for acceleration with the current thrust, weight, drag, and the previous time step's velocity, an Eulerian integration method is used to find the velocity after one-half time step. Typically, Runge-Kutta is sufficient on its own, but given the nature of this problem, it requires the extra integration on velocity, and Euler is sufficient. The new velocity is used to determine the drag after one-half time step, used in Eq. 20 to find the second estimate for acceleration. Those steps are repeated for Eq. 21-22, finding the velocity at time steps from the most recent acceleration estimate, then finding the drag and the subsequent acceleration. After the 4 estimates have been found, Eq. 23 finds the best estimate. The Eq. 23 result is used in the Eulerian integration method to find the velocity, shown in Eq. 24.

$$v_{n+1} = v_n + k_n(dt) \quad \text{Eq. 24}$$

With the acceleration and the velocity now derived, Newton's equation of motion (Eq. 25) is used to determine the change in height. Note that the velocity from Eq. 24 and the acceleration from Eq. 23 are used.

$$z_{n+1} = z_n + v_{n+1}(dt)sin(\theta) + \frac{1}{2}k_n dt^2 sin(\theta) \quad \text{Eq. 25}$$

The range, or horizontal distance, uses Eq. 25 as well, except the directionality of the change is from $cos(\theta)$ instead of $sin(\theta)$. The only addition to this process is determining the change in θ which will be outlined in section 3.2. Otherwise, this entire process is repeated until the propellant mass has run out.

3.2. Coasting Phase

The coasting phase uses the same procedure as the powered ascent, except that the thrust is now zero and the weight is no longer changing. Therefore, the only forces now acting on the rocket are weight and drag. The drag and velocity are still dependent on θ and ψ, though, so there is still some general complexity involved. The sideslip angle, ψ, results from the rocket pitching into the wind resulting in a momentary angle between the thrust vector and the direction of motion. Recall from section 2.39 that the stability margin is the distance between the CP and the CG. Wind contributes to the lift force on the rocket, which acts through the CP, creating torque and subsequent pitch dependent on the stability margin as a moment arm. Unfortunately, the exact torque created by the wind on the rocket is challenging to determine as a function of stability margin, so the process of simulating this effect is simplified.

$$\psi = tan^{-1}\left(\frac{v_n sin(\theta)}{v_n cos(\theta) + v_w}\right) \quad \text{Eq. 26}$$

Eq. 26 finds the sideslip angle with respect to horizontal by adding the relative velocity of the wind, v_w, to the horizontal rocket velocity. The assumption is that the wind acts only parallel to the ground. The sideslip angle as a function of crosswind velocity is used to determine the change in θ. The change in theta is found by assuming the acceleration in the direction perpendicular to the flight path is centrifugal, shown in Eq. 27. Note that the change in θ, is entirely dependent on the weight. The theta for each time step is derived by using the Eulerian integration method shown in Eq. 24, with θ_n and $d\theta$.

$$mv\frac{d\theta}{dt} = Tsin(\psi - \theta) - mgcos(\theta) \quad \text{Eq. 27}$$

For even better accuracy, the wind is not assumed to be constant. Eq. 28, [3], shows the model for calculating wind speed at altitude given a measured wind speed at a known altitude. α represents the wind shear exponent, based on the terrain surrounding the launch pad.

$$v_2 = v_1\left(\frac{z_2}{z_1}\right)^{\alpha} \quad \text{Eq. 28}$$

Figure 10 shows an example of wind speed changing with altitude based on the validation rocket scenario. The initial velocity was measured as 2 mph at 32.8 ft.

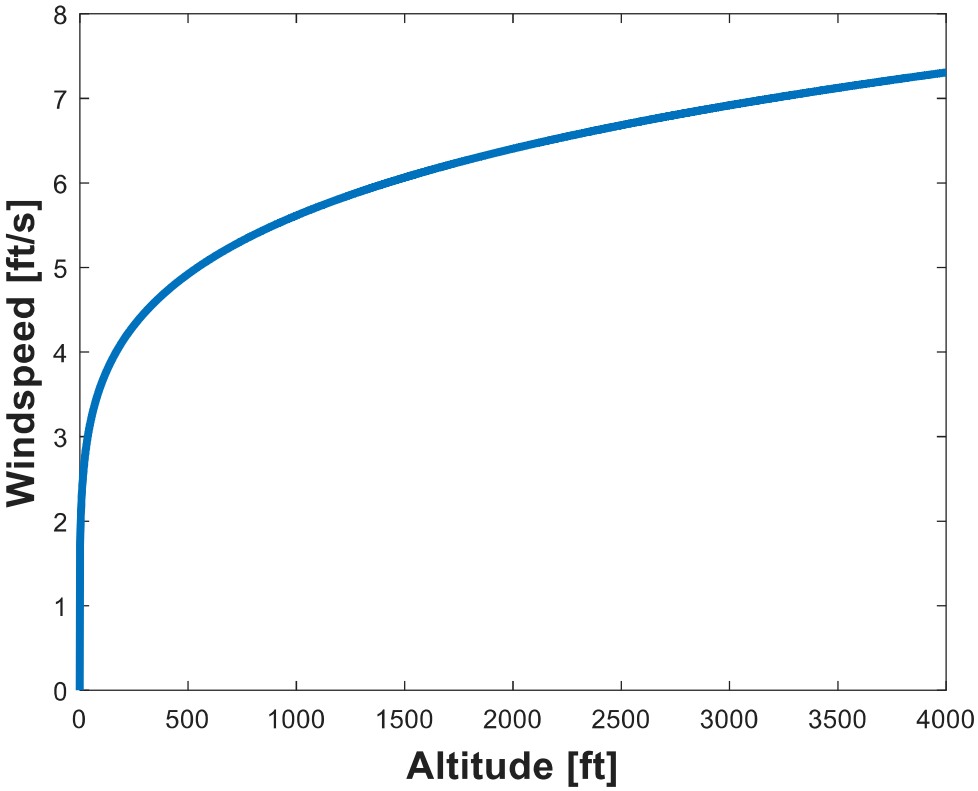

Figure 10: Windspeed model

The other significant variable is the change in air density with height. Because the dependent variable for the air density is the altitude which is an independent variable of time, a lagrangian interpolation can not be used on the air density. Instead, a model similar to the windspeed was created to approximate a function that fits reference data. The reference data used was the international standard atmosphere density data [9].

$$\rho = \rho_o e^{-3.09 \cdot 10^{-5} z} \qquad \text{Eq. 29}$$

Eq. 29 is the resulting model. ρ_o represents the initial density in $lb\backslash ft^3$ as measured by the international atmospheric data, and z is the current altitude. A comparison between the model output and the ISA data is shown in Figure 11.

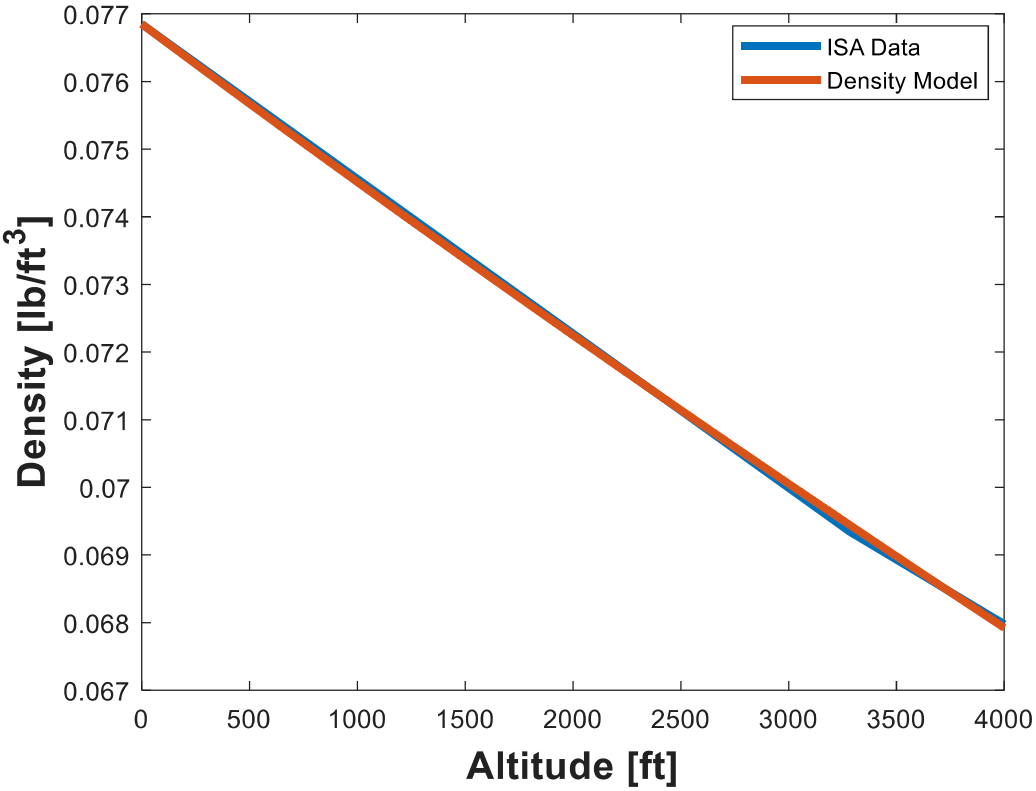

Figure 11: Density Model

As mentioned, the process for iterating the altitude is almost identical with the powered ascent phase, neglecting thrust as the motor has burned out. Ultimately, the opposing forces reduce the velocity, at which point the rocket has reached its apogee.

3.3. Recovery

As mentioned in Section 2, this document deals with rockets using a dual recovery system. A smaller drogue parachute is deployed at apogee, and a larger main parachute is deployed at some lower altitude. The parachute's purpose is to reduce the descent rate of the rocket as it comes back towards the ground resulting in minimal impact energy. For simplification, while iterating the flight profile, the parachute drag is assumed to be instantaneous. Eq. 18 is used with the cross-sectional area as the nominal cross-sectional area of the parachute, and C_d is the nominal drag coefficient of the parachute.

By nature, a parachute can quickly reach its terminal velocity based once the drag force contribution is equal to that of the weight. Therefore, assuming immediate deployment does not take much away from the accuracy of the simulation. However, a significant concern during the recovery phase is the forces put on the recovery harness connections because of a near-instantaneous change in momentum. In Eq. 30, the right-hand side of the equation is finite and nonzero because the mass is constant, and the change in velocity is the difference between the initial velocity before the parachute is deployed. The terminal velocity after the parachute is

deployed. However, assuming an immediate deployment means dt on the left-hand side is approaching zero, meaning F must approach infinity. An infinite force is unrealistic for a parachute deployment impulse load, allowing the spike in acceleration to be ignored. However, the actual loads need to be characterized to better approximate how robust the recovery harness linkages need to be.

$$\int \mathrm{Fdt} = \int \mathrm{mdv} \qquad \text{Eq. 30}$$

The impulse load of a parachute deployment is a function of [5]:

a. Type of parachute
b. Instantaneous weight (assumed constant)
c. Nominal parachute drag area
d. Canopy rate of airflow
e. Operational altitude
f. Instantaneous velocity

Because the instantaneous velocity of the drogue deployment is assumed to be zero at apogee, the change in velocity is minimal. Therefore, the simulation only calculates the expected impulse load for the main parachute deployment. The main parachute from the validation rocket is assumed to be a 96-inch diameter, 12 gore hemispherical, solid, MIL-C-7020, Type III cloth parachute with no vent. This assumption minimizes the parachute material's assumed permeability, meaning the parachute opens quicker and provides a larger expected impulse load. The larger load estimate is chosen as a factor of safety. The weight of the rocket at deployment is about 44.7 lbs. The nominal parachute drag area is the cross-sectional area of the circular base using the area for a perfect circle, i.e., assuming there is no stretching of the parachute opening, which is $50.3 ft^2$. The operational altitude is 600 ft; however, to continue maximizing the expected force, the air density at sea level is used. The canopy rate of airflow and the instantaneous velocity factor into the reference time when the parachute has reached the nominal drag area for the first time.

$$t_o = \frac{14W}{V_s \rho g C_d S_o}\left[e^{\frac{g\rho V_o}{2W}\left[\frac{C_d S_o}{A_{mo} - A_{so} k\left(\frac{C_p \rho}{2}\right)^n}\right]} - 1\right] \qquad \text{Eq. 31}$$

Table 5 describes the parameters in Eq. 31 with values from the validation rocket.

Table 5: Parachute deployment load parameters

Parameter	Description	Value
V_s	System Velocity after shock cord stretch	$-70.6\frac{ft}{s}$
S_o	Canopy Surface Area	$50.27\ ft^2$
V_o	System Velocity at t = to	$68.6\frac{ft}{s}$
A_{mo}	Steady State inflated mouth area	$19.2\ ft^2$
A_{so}	Canopy Surface Area	$50.27\ ft^2$
k	Permeability Constant	1.46042
n	Permeability Constant	0.57403
C_p	Coefficient of Pressure	1.7

For the validation rocket, t_o is 0.43 s. The next step is to determine at what point, relative to the 0.43 seconds, that the parachute reaches its maximum impulse load. A new parameter, the Ballistic Mass Ratio (BMR), M, is used to find the percentage of the maximum possible force based on t_o. Eq. 32 shows the calculation for the BMR, M.

$$\mathrm{M} = \frac{2\mathrm{W}}{\rho \mathrm{g} \mathrm{V_s} \mathrm{t_o} \mathrm{C_d} \mathrm{S_o}} \qquad \text{Eq. 32}$$

Using M, the time at maximum loading can be calculated using Eq. 33. Subsequently, the percentage of the maximum possible force expected to be exhibited by the parachute opening can be found using Eq. 34.

$$\mathrm{t} = \mathrm{t_o}\left(\frac{21\mathrm{M}}{4}\right)^{1/7} \qquad \text{Eq. 33}$$

$$\mathrm{x_{imax}} = \frac{16}{49}\left(\frac{21\mathrm{M}}{4}\right)^{6/7} \qquad \text{Eq. 34}$$

The maximum possible force uses Eq. 18 to determine the drag force but assumes the rocket is traveling at the terminal velocity under the drogue parachute, meaning each parameter is maximized. When this force and the percentage expected are combined, the result is Eq. 35.

$$F_{max} = x_{i_{max}}\left(\frac{1}{2}\rho V_s^2 C_d S_o\right) \quad \text{Eq. 35}$$

Using the validation rocket, with $x_{i_{max}} = 0.55$, the maximum force expected was 357 lbs or 11.1 gs.

3.4. Results

A prediction was made for three separate rocket launches and then compared to the flight data recorded by altimeters onboard the rocket using the outlined process from Sections 3.1-3.3. The first flight was with the validation rocket, whose parameters were outlined in Table 2. The launch conditions were an ambient temperature of 74 degrees Fahrenheit and measured crosswinds of 7 mph at an altitude of 32.8 feet. The initial launch rod angle was one degree from vertical, which means the initial θ was 89 degrees. One source of measuring the actual flight data was used to compare with the simulation prediction. The results are shown in Figure 12.

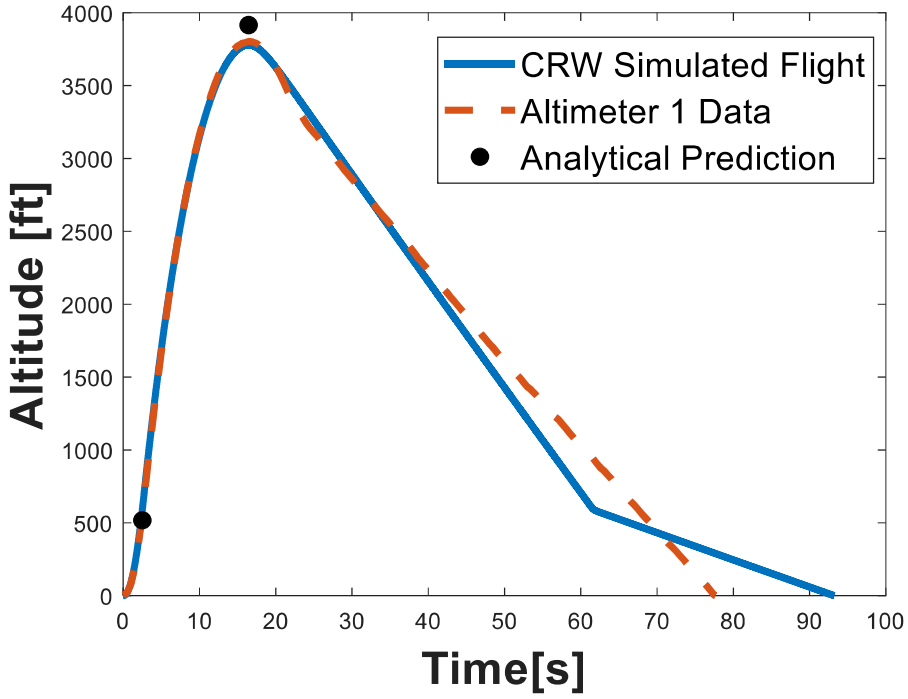

Figure 12: First Comparison/Validation Flight

In Figure 12, the analytical predictions for burnout height and apogee are plotted with black dots. The burnout height for all three methods, analytical, simulation, and actual flight data, compares very well. However, the analytical expectation for apogee, 3915 ft, is much higher than the

simulation, 3750 ft, and the actual flight data, 3805 ft. This discrepancy reveals the danger of relying on the analytical solution as the vertical flight assumption or even a predetermined angle of attack assumption is not conducive to real-world conditions like wind. More importantly, the simulation compares very well with the actual flight data. The recovery phase has significant discrepancies between the actual flight and the simulation due to recovery system issues on the actual flight.

The second flight was used to compare the simulation and real data using the same rocket from the validation flight with a 0.5 lbs increase in weight. The launch conditions were an ambient temperature of 78 degrees Fahrenheit and measured crosswinds of 12 mph at an altitude of 32.8 feet, with a launch rail angle of 1 degree. The wind is significantly higher for the second flight, meaning the rocket is expected to experience greater pitch and subsequently a lower apogee. The flight profile is shown in Figure 13.

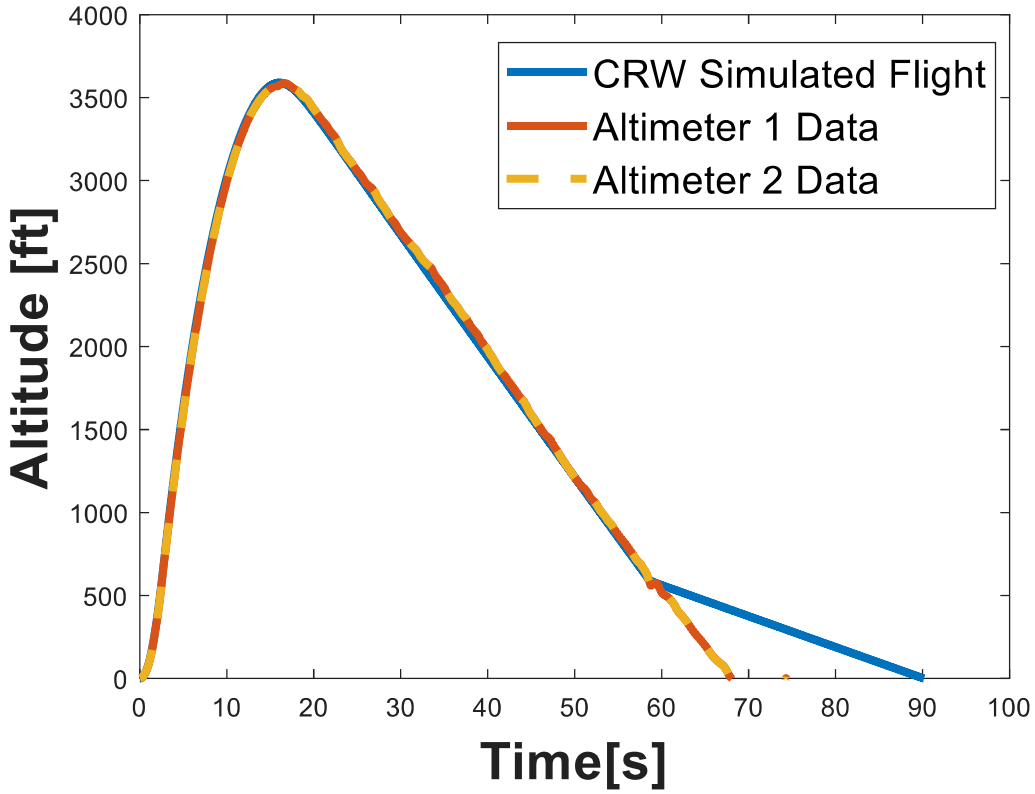

Figure 13: Second Comparison Flight

The second flight had an additional altimeter on board for measuring the actual apogee; both altimeters measured an apogee of 3587 ft, with the simulation predicting an apogee of 3590 ft. There were also issues with the recovery system on the actual flight, but the simulation is validated through the drogue parachute portion of the recovery phase.

The third comparison flight used a similar rocket as the first two in that the diameter and motor were the same. The differences were a weight of 53 lbs, a length of 117 inches, and a drag

coefficient of 0.53. The launch conditions were an ambient temperature of 76 degrees Fahrenheit and measured crosswinds of 5 mph at an altitude of 32.8 feet, with a launch rail angle of 2 degrees. The flight profile is shown in Figure 14.

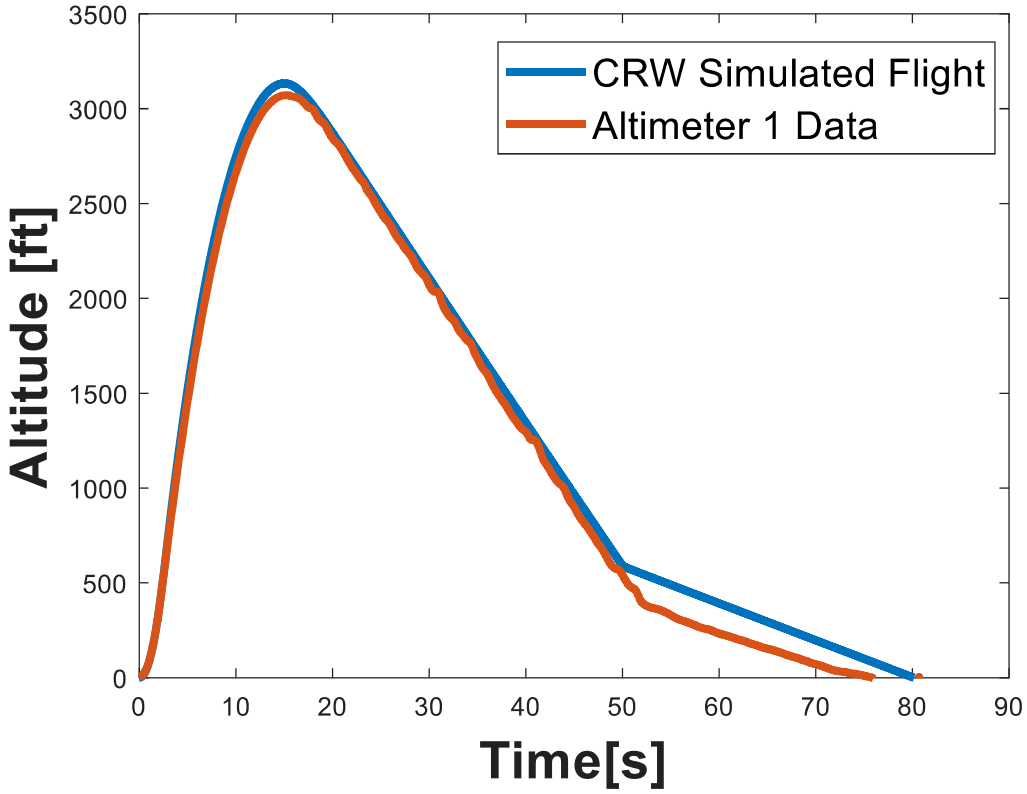

Figure 14: Third Comparison Flight

The simulation predicted an apogee of 3134 ft, and the maximum recorded apogee was 3078 ft. The actual rocket flight had a delayed main parachute deployment; however, the descent rate provided by the main parachute was validated by this flight.

4. Simulation Monte Carlo Analysis

As mentioned, the simulation was designed to be as accurate as possible. That does not mean the mission-critical parameters outputted by the simulation are always perfect. The pursuit of accuracy is only to narrow the standard deviation on how well the simulation can match a nominal flight. However, a nominal flight is relatively improbable. Therefore, any predictions made based on the nominal outcome of the simulation are likely to be incorrect. To that effect, a confidence interval needs to be built around the expectation to provide a more accurate understanding of a realistic flight. A Monte Carlo simulation was chosen to provide the uncertainty intervals of various parameters listed in Table 6.

Table 6: Uncertainty parameters and ranges

Parameter	Range
Mass	$\pm 2\%$
Rocket Diameter	$\pm 0.01\ in.$
Drag Coefficient	± 0.05
SSL air density	$\pm 0.001 \frac{lb}{ft^3}$
Thrust	$\pm 2\%$
Wind	$\pm 2\ mph$
Wind Coefficient	± 0.1

Each parameter is designed to capture its effect on the rocket's performance and effects of parameters not listed. For instance, the standard sea-level air density and wind have uncertainty to predict the effects of the ambient weather conditions and potential unexpected deviations from the models described in Section 3.2. The drag coefficient similarly captures varying weather conditions such as viscosity changes due to temperature changes and changes in humidity. The drag coefficient also captures unaccounted for abrasions and protuberances on the rocket. The rocket diameter, mass, and thrust account for uncertainty in the manufacturing of purchased material. The rocket's body tubes could vary in diameter from their manufacturer's described nominal diameter. The rocket motors could have different amounts of propellant, which affects both mass and thrust. In summation, the list of parameters in Table 6 is not comprehensive in terms of parameters with uncertainty. However, it is intended to be comprehensive in terms of the effect on the rocket's performance.

The ranges are set to follow a normal probability density allowing the expectation to be concentrated around the nominal outcome with normal distribution. To correctly apply the Monte Carlo method, each distribution must be random, meaning the parameters do not align in terms of deviation from their nominal values. The simulation is then repeated a sufficient number of times using the randomly generated parameter values from each of their distributions for each iteration of the simulation. Figure 15 shows the outcome of 100,000 simulations performed on the second comparison flight's rocket (Figure 13).

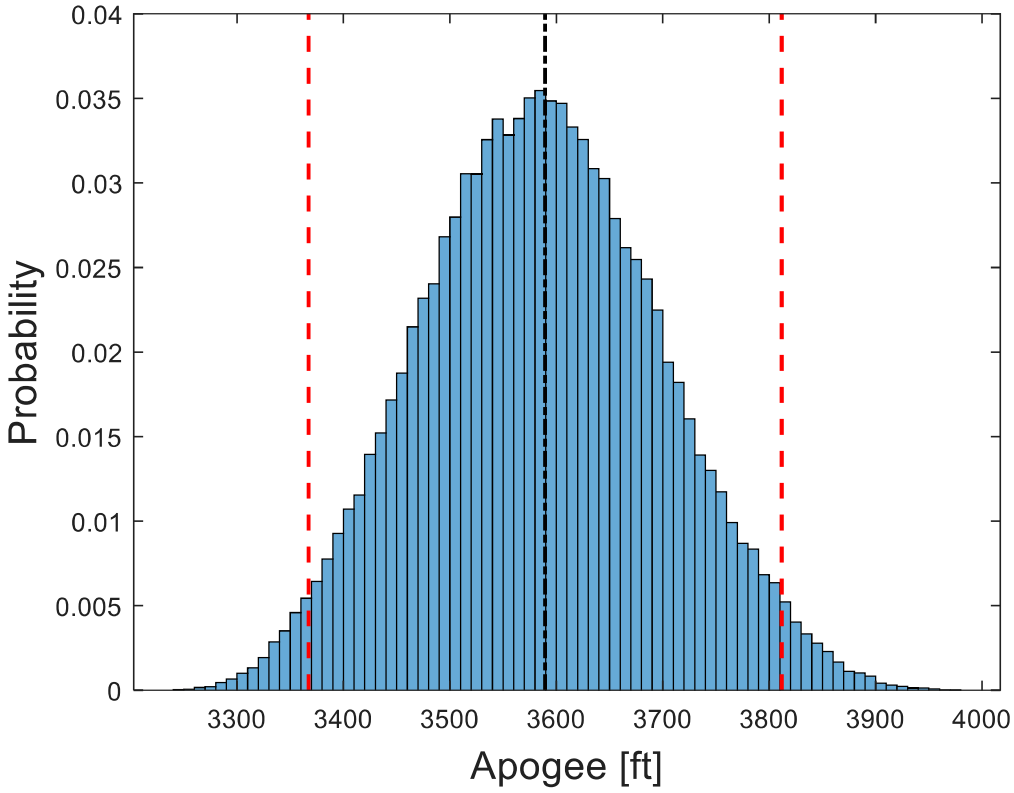

Figure 15: Monte Carlo distribution of 100k rocket flights

The result of the Monte Carlo simulation is a normally distributed probability density about the nominally expected apogee. The confidence interval represented by the red lines in Figure 15 provides a 95.7% probability that the second comparison flight's apogee would be between 3366 and 3813 ft.

5. Conclusion

The purpose of this project was to create a numerical simulation of a high-powered rocket's flight profile using Matlab to capture its performance expectation more accurately. Additionally, a Monte Carlo uncertainty analysis was integrated to account for unpredictable flight variables such as weather conditions and variability in the rocket's design. The simulation was compared against three separate actual flights of a rocket. The result was a maximum percent error of 1.8% for the apogee expectation and negligible error for burnout height and burnout velocity. This result shows good accuracy for predicting the outcome of a nominal flight with known parameters. The Monte Carlo results in Figure 15 show good simulation precision as the apogee expectations are normally distributed around the nominal value.

The next step would be making this simulation better suited for different rockets. Currently, most of the rocket parameters are hardcoded into the Matlab script, meaning for changes to the rocket, those lines of code would need to be adjusted. A more accessible solution would be to read in parameters from a separate file, so their location is readily available. The program could

also be made more accurate by implementing more degrees of freedom. A team building a rocket may be tasked with controlling its flight, requiring a working knowledge of how the rocket responds in those control areas. For instance, a team controlling the roll of the rocket would require this simulation to predict the roll characteristics and provide uncertainty for those characteristics. Ultimately, this simulation could be used to fully characterize all aspects of any rocket's flight with relatively simple user requirements.

6. Works Cited

1. Barrowman, James S, and Judith A Barrowman. “The Theoretical Prediction of the Center of Pressure.” *Apogee Rockets*, www.apogeerockets.com/downloads/barrowman_report.pdf.
2. Heister, Stephen D., et al. *Rocket Propulsion*. Cambridge University Press, 2019.
3. *Katabatic Power*, websites.pmc.ucsc.edu/~jnoble/wind/extrap/.
4. “Lagrange Method of Interpolation – More Examples Computer Engineering .” *Http://Nm.mathforcollege.com/Strippedfiles/Mws/Com/05inp/mws_com_inp_txt_lagrange_examples.Pdf*.
5. Ludtke, William P. *Observations on the Inflation Time and Inflation Distance of Parachutes*. apps.dtic.mil/sti/pdfs/ADA221167.pdf.
6. Niskanen, Sampo. *OpenRocket Technical Documentation*. openrocket.sourceforge.net/techdoc.pdf.
7. *Project Bellerophon Final Design Report*. engineering.purdue.edu/AAECourses/aae450/2008/spring/S08_Main.pdf.
8. Nakka, Richard A. Simplified Method for Estimating the Flight Performance of a Hobby Rocket. Mar. 2007, www.nakka-rocketry.net/articles/altcalc.pdf.
9. Engineering ToolBox, (2005). International Standard Atmosphere. [online] Available at: https://www.engineeringtoolbox.com/international-standard-atmosphere-d_985.html